Electronic Supplementary Information

Band Engineering in Iron and Silver Co-Doped Double Perovskite Nanocrystals for Selective Photocatalytic CO_2 Reduction

Razi Ahmad[1*], Yu Zhang[1], Jan Navrátil[1,2], Piotr Błoński[1,5], Lukáš Zdražil[1,6], Sergii Kalytchuk[1], Alberto Naldoni[1,3*], Andrey L. Rogach[4,5], Michal Otyepka[1,5], Radek Zboril[1,6*], and Štěpán Kment[1,6*]

[1]Regional Centre of Advanced Technologies and Materials, Czech Advanced Technology and Research Institute, Palacký University Olomouc, Šlechtitelů 27, Olomouc, 783 71, Czech Republic

[2]Department of Physical Chemistry, Faculty of Science, Palacký University Olomouc, 17. listopadu 1192/12, 779 00 Olomouc, Czech Republic

[3]Department of Chemistry and NIS Centre, University of Turin, Turin 10125, Italy

[4]Department of Materials Science and Engineering, and Center for Functional Photonics (CFP), City University of Hong Kong, 83 Tat Chee Avenue, Hong Kong S.A.R., China

[5] IT4Innovations, VŠB – Technical University of Ostrava, 17. listopadu 2172/15, 708 00 Ostrava-Poruba, Czech Republic

[6]Nanotechnology Centre, Centre for Energy and Environmental Technologies, VŠB–Technical University of Ostrava, 17. listopadu 2172/15, 708 00 Ostrava-Poruba, Czech Republic

Corresponding Authors:

stepan.kment@upol.cz, radek.zboril@upol.cz, razi.ahmad@upol.cz,

alberto.naldoni@unito.it

EXPERIMENTAL SECTION

Extraction and Purification of NCs. The extraction and purification of NCs from as-synthesized crude solution was performed by antisolvent washing method with methyl acetate (MA). The photographs of each washing step are presented in Figure S1. In brief, 2 mL of crude solution was mixed with 6 mL of MA, which resulted in a turbid mixture due to precipitation of NCs. The turbid mixture was shaken and kept for few minutes so that the precipitated NCs settled down at the bottom of the centrifuge tube. After that, 90% of supernatant was removed and then again 6 mL of MA was added to the precipitated NCs. The above steps were repeated three times in order to remove the excess residual organics such as unbound ligands and ODE. Finally, the purified NCs were collected through centrifugation at 3000 rpm for 5 min and redispersed in 2 mL of toluene, which resulted in an optical clear colloidal solution (Figure S1).

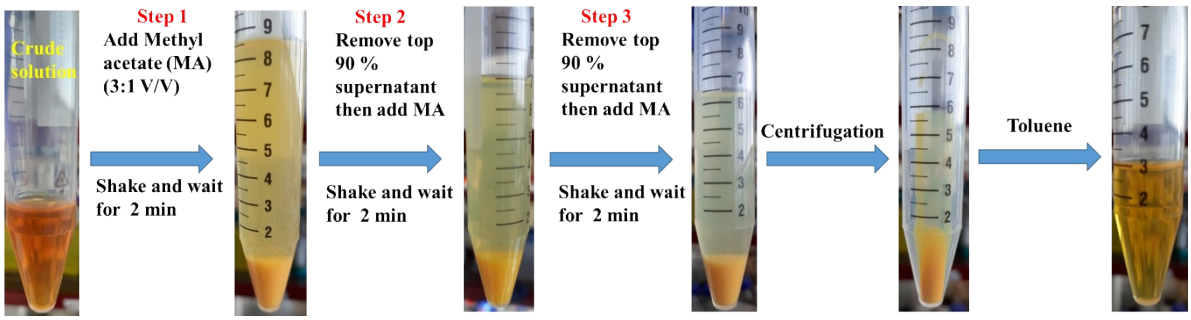

Figure S1. Photographs of extraction and purification processes of Fe^{3+}-doped $Cs_2Ag_{0.5}Na_{0.5}InCl_6$ NCs

Characterization: The phase purity and the crystal structure of the NCs were analysed by an X'Pert PRO MPD powder diffractometer (PANalytical) using iron-filtered Co source with Kα radiation (λ = 0.1789 nm) at 40 kV and 30 mA. Samples for XRD measurements were made from concentrated NC suspensions in toluene and by drop casting onto a zero-diffraction silicon single crystal substrate followed by drying naturally in air at room temperature. Elemental compositions of NCs were analyzed by Agilent 7700x ICP-MS spectrometer. Samples for ICP-MS measurements were prepared by digesting 5 mg of dried NCs powder in 1 mL HNO_3/HCl mixture (1:3 v/v) under sonication, followed by dilution with deionized water. The XPS measurements were carried out with a PHI Versa Probe II (Physical Electronics) spectrometer using an Al Kα source (15 kV, 50 W). EPR spectra were recorded on a JEOL JES-X-320 spectrometer operating at the X-band frequency (~9.0–9.1 GHz) equipped with a variable-temperature controller (He, N_2) ES-CT470 apparatus. The TEM analysis of antisolvent

washed NCs was performed by using a JEOL microscope with a LaB_6 emission gun operated at an accelerating voltage of 200 kV. Samples were prepared from dilute NC solution in toluene by dropping 10 µL solution onto a carbon-coated Cu grid and drying it in air at room temperature. High-angle annular dark-field (HAADF) scanning TEM (STEM) imaging and STEM energy dispersive X-ray spectroscopy (EDS) elemental mapping were performed on a FEI Titan G2 HRTEM with X-FEG electron gun at an accelerating voltage of 80 kV. The UV-Vis absorption spectra were collected on a Specord S600 UV-Vis spectrophotometer (Analytik Jena). Steady-state photoluminescence (PL) spectra were acquired on a FLS980 fluorescence spectrometer (Edinburgh Instruments) equipped with a 450 W xenon arc lamp as the excitation source. The PL lifetime analysis was performed by time-correlated single-photon counting using the same spectrophotometer. The pulsed laser diode (EPL-375) with excitation wavelength of 372 nm, pulse width 66.5 ps, pulse repetition rate of 10 MHz and an average power of 75 µW were used as an excitation source for nanosecond PL lifetime measurements while for microsecond range, a µF920H Xenon flash lamp were used. ^{1}H and ^{31}P NMR spectra of NC solutions were recorded on a 400 MHz NMR JEOL spectrometer. The CO_2 adsorption capacity of catalyst was determined by CO_2 absorption/desorption measurement on Quantachrome instrument gas adsorption analyser. The photoelectrochemical measurements were carried out at a Gamry potentiostat Series G 300 (Gamry Instruments, Warminster, PA, USA) with three electrode configuration cell, including the working electrode (NCs film on FTO glass), the Pt counter electrode and Ag / AgCl (in 3M KCl) as the reference electrode. The ethyl acetate solution of 0.1 M tetrabutylammonium hexafluorophosphate ($TBAPF_6$) was used as electrolyte. The transient photocurrent density (I-t) was recorded at -0.4 V vs Ag/AgCl under 150 mW cm^{-2} Xe light illumination. The electrochemical impedance spectra were collected at the open circuit condition under similar illumination. The ^{13}C isotope labelling experiment was performed by using $^{13}CO_2$ as the feedstock gas. The gaseous products were analysed on a gas chromatograph-mass spectrometry (GC–MS, QP2010 SE, Shimadzu, Kyoto, Japan).

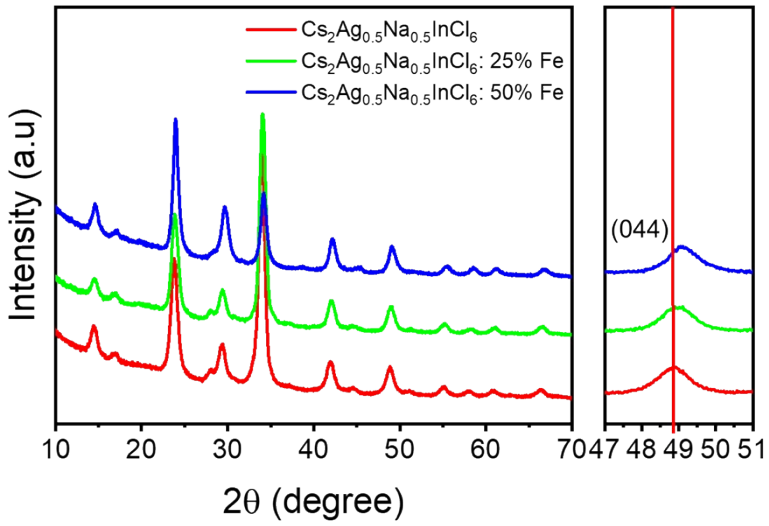

Figure S2: XRD patterns of undoped and Fe^{3+}-doped $Cs_2Ag_{0.5}Na_{0.5}InCl_6$ NCs. The right panel shows an enlarged view of the (044) diffraction peak of the prepared samples.

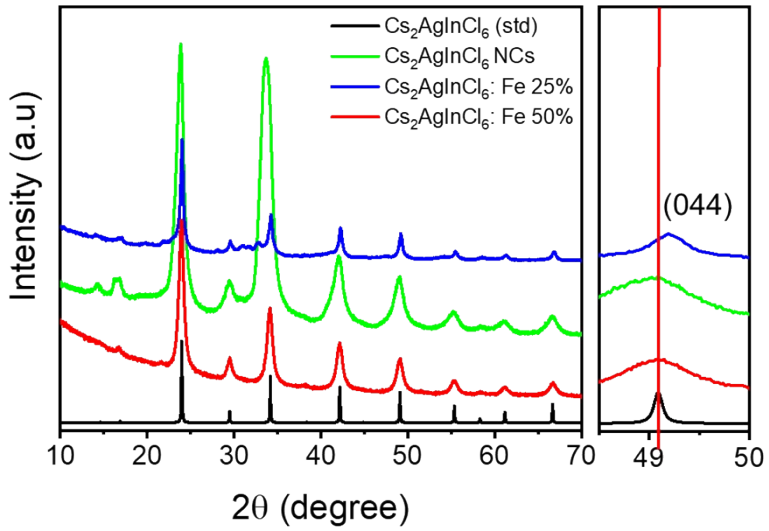

Figure S3: XRD patterns of undoped and Fe^{3+}-doped $Cs_2AgInCl_6$ NCs, with corresponding reflections of bulk $Cs_2AgInCl_6$ marked as (std) The right panel shows an enlarged view of the (044) diffraction peak of the prepared samples.

Table S1. ICP-MS analysis of Fe^{3+}-doped $Cs_2NaInCl_6$ NCs.

Feeding ratio Fe (x)	Na (mg/L)	In (mg/L)	Fe (mg/L)	Na (mmol/L)	In (mmol/L)	Fe (mmol/L)	Na/In+Fe	Fe/In+Fe (%)
0	165.33	860.16	0.00	7.18	7.47	0.00	0.96	0.0
0.25	166.72	794.64	34.14	7.24	6.90	0.61	0.96	8.1
0.50	194.56	747.33	102.48	8.45	6.50	1.83	1.00	21.8

Table S2. ICP-MS analysis of Fe^{3+}-doped $Cs_2Ag_{0.5}Na_{0.5}InCl_6$ NCs.

Feeding ratio Fe (x)	Na (mg/L)	In (mg/L)	Fe (mg/L)	Na (mmol/L)	In (mmol/L)	Fe (mmol/L)	Na/In+Fe	Fe/In+Fe (%)
0	66.72	781.81	0.00	2.90	6.81	0.00	0.42	0.0
0.25	75.16	634.25	10.89	3.26	5.51	0.19	0.51	3.4
0.50	89.82	609.07	37.47	3.90	5.23	0.67	0.66	11.3

Table S3. ICP-MS analysis of Fe^{3+}-doped $Cs_2AgInCl_6$ NCs.

Feeding ratio Fe (x)	In (mg/L)	Fe (mg/L)	In (mmol/L)	Fe (mmol/L)	Fe/In+Fe (%)
0	772.08	0.00	6.71	0.00	0.0
0.25	799.43	3.10	6.95	0.05	0.8
0.50	519.07	5.53	4.51	0.10	2.1

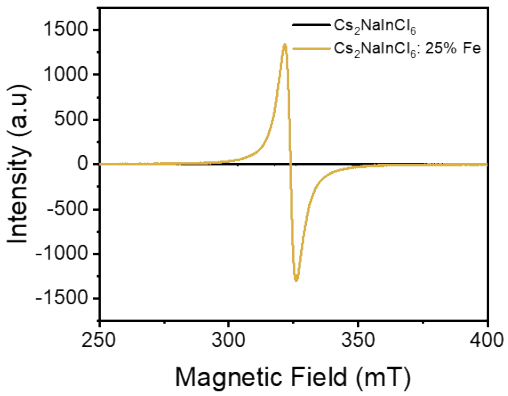

Figure S4: EPR signals of undoped $Cs_2NaInCl_6$ and Fe^{3+}-doped $Cs_2NaInCl_6$ NCs with a nominal 25% Fe amount, measured at room temperature.

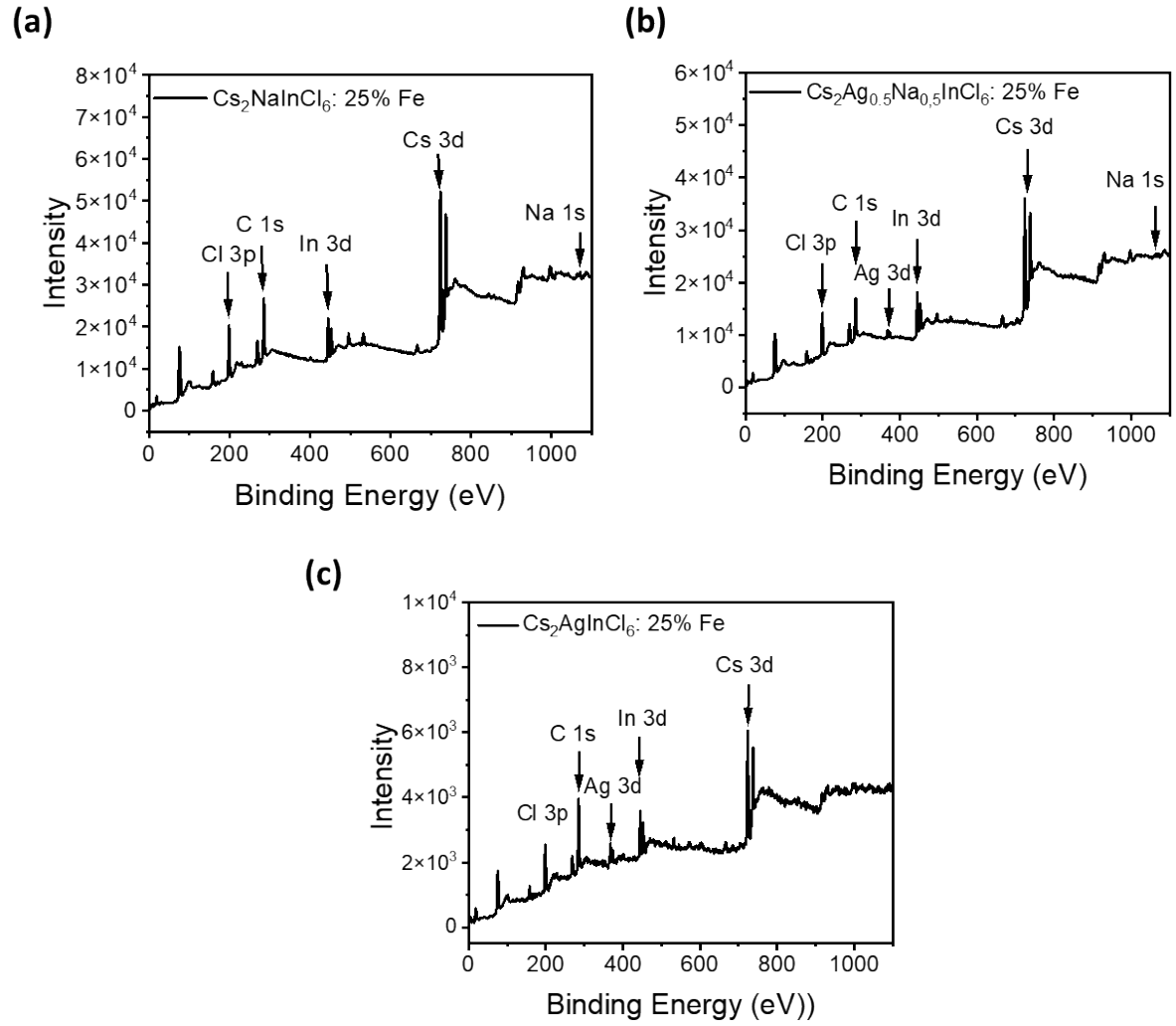

Figure S5: XPS survey spectrum of Fe^{3+}-doped (a) $Cs_2NaInCl_6$, (b) $Cs_2Ag_{0.5}Na_{0.5}InCl_6$, and (c) $Cs_2AgInCl_6$ NCs.

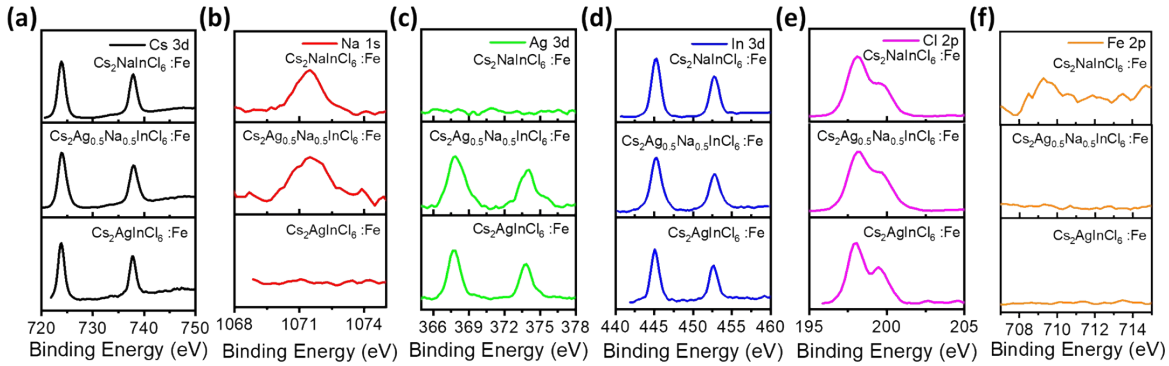

Figure S6: High-resolution XPS spectra for (a) Cs 3d, (b) Na 1s (c) Ag 3d, (d) In 3d, (e) Cl 3p, and (f) Fe 2p of Fe^{3+}-doped (25% nominal Fe^{3+} loading with respect to In) $Cs_2Ag_xNa_{1-x}InCl_6$ (x = 0, 0.5 and 1) NCs.

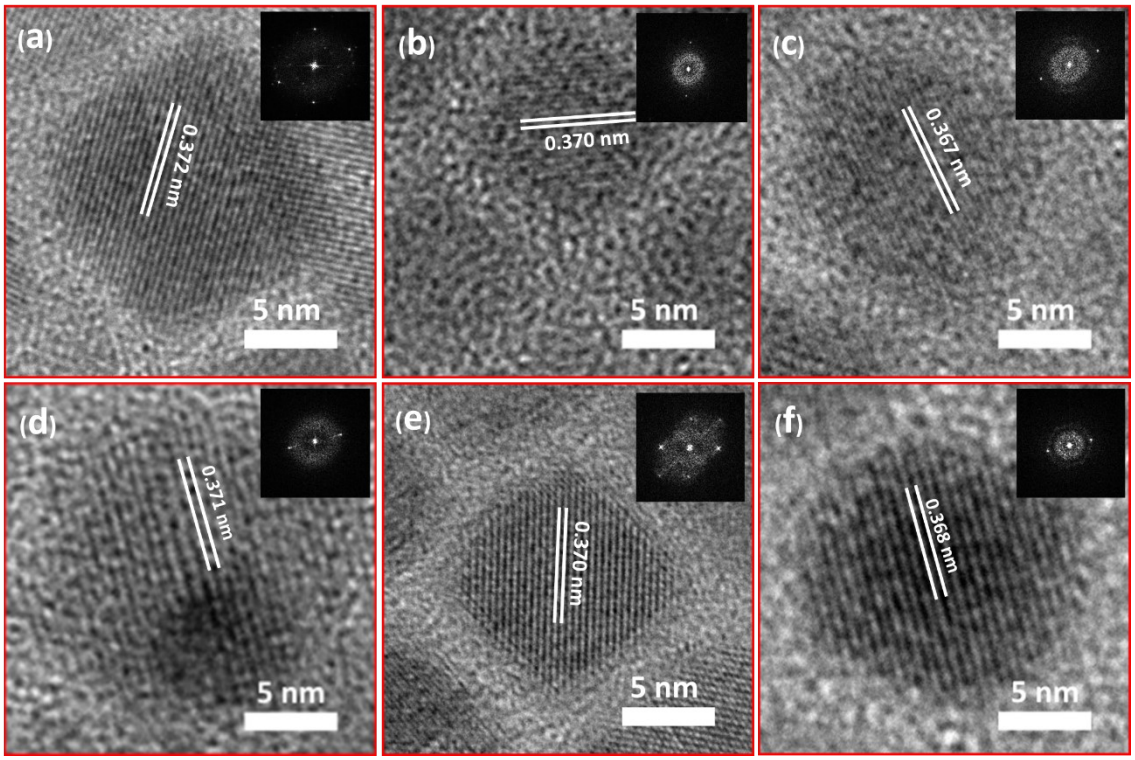

Figure S7: HRTEM images and their corresponding FFT patterns (inset) of (a) undoped and Fe^{3+}-doped $Cs_2NaInCl_6$ NCs with feeding molar ratio of (b) 25% (c) 50%. HRTEM images and their corresponding FFT patterns (inset) of (d) undoped and Fe^{3+}-doped $Cs_2Ag_{0.5}Na_{0.5}InCl_6$ NCs with feeding molar ratio of (e) 25% (f) 50%.

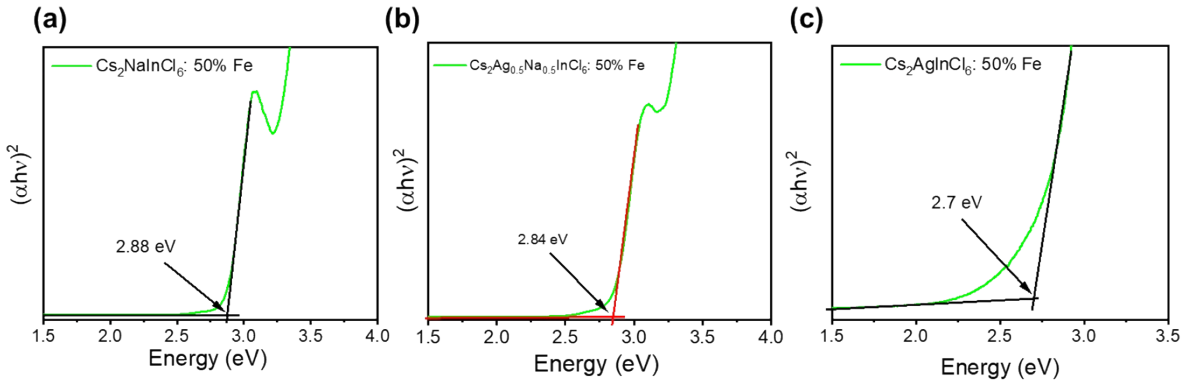

Figure S8. Tauc plots of Fe^{3+}-doped samples with a nominal iron amount of 50%. (a) $Cs_2NaInCl_6$, (b) $Cs_2Ag_{0.5}Na_{0.5}InCl_6$, and (c) $Cs_2AgInCl_6$ NCs, respectively.

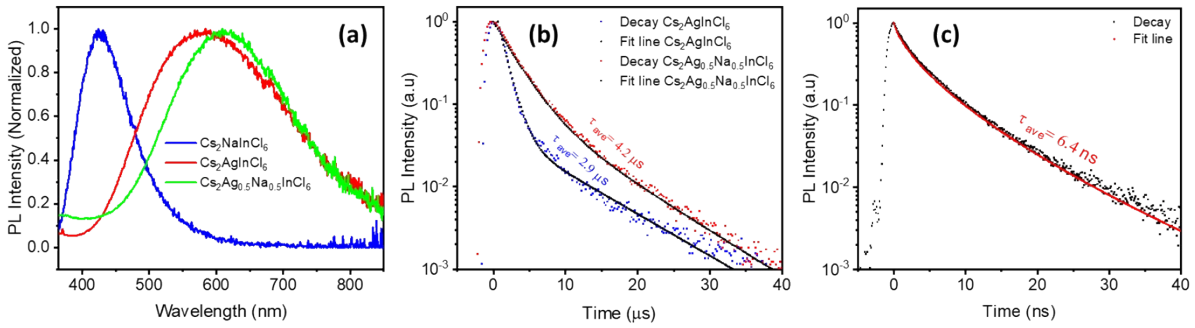

Figure S9. (a) PL spectra of undoped $Cs_2NaInCl_6$ (blue curve), (red curve) (red curve), and $Cs_2Ag_{0.5}Na_{0.5}InCl_6$ (green curve) nanocrystals. (b) Time resolved PL spectra of $Cs_2AgInCl_6$ NCs (blue dots) and $Cs_2Ag_{0.5}Na_{0.5}InCl_6$ NCs (red dots); solid lines represent two-exponential fits. (c) Time resolved PL spectra of $Cs_2NaInCl_6$ NCs.

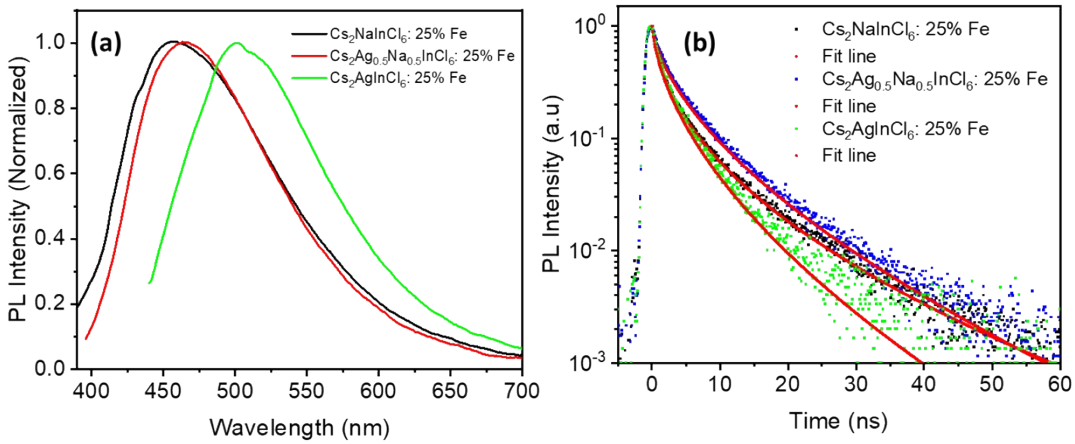

Figure S10. (a) PL spectra of Fe^{3+}-doped (25% nominal Fe^{3+} loading with respect to In) $Cs_2NaInCl_6$ NCs (black curve), $Cs_2Ag_{0.5}Na_{0.5}InCl_6$ NCs (red curve), and $Cs_2AgInCl_6$ NCs. (b) Time resolved PL spectra of Fe^{3+}-doped (25% nominal Fe^{3+} loading with respect to In) $Cs_2NaInCl_6$ NCs (black dots), $Cs_2Ag_{0.5}Na_{0.5}InCl_6$ NCs (blue dots), and $Cs_2AgInCl_6$ NCs (green dots); solid red lines represents tri-exponential fits.

Table S4. Fitting parameters for microsecond PL decay curves of undoped $Cs_2AgInCl_6$ and $Cs_2Ag_{0.5}Na_{0.5}InCl_6$ NCs.

Composition	B_1 (%)	τ_1 (µs)	B_2 (%)	τ_2 (µs)	τ_{av} (µs)
$Cs_2AgInCl_6$	77.1	1.1	22.9	8.6	2.9
$Cs_2Ag_{0.5}Na_{0.5}InCl_6$	70.7	2.6	29.3	8.0	4.2

Table S5. Fitting parameters for nanosecond PL decay curves of Fe^{3+}-doped samples with a nominal iron amount of 25%, and undoped $Cs_2NaInCl_6$ NCs.

Composition	B_1 (%)	τ_1 (ns)	B_2 (%)	τ_2 (ns)	B_3 (%)	τ_3 (ns)	τ_{av} (ns)
$Cs_2NaInCl_6$: Fe	16.6	0.8	45.3	3.5	39.0	11.8	6.2
$Cs_2Ag_{0.5}Na_{0.5}InCl_6$: Fe	13.5	1.1	50.5	4.4	35.8	12.2	6.8
$Cs_2AgInCl_6$: Fe	18.4	0.9	54.0	3.3	27.5	10.0	4.7
$Cs_2NaInCl_6$	11.8	1.2	59.5	4.6	28.6	12.4	6.4

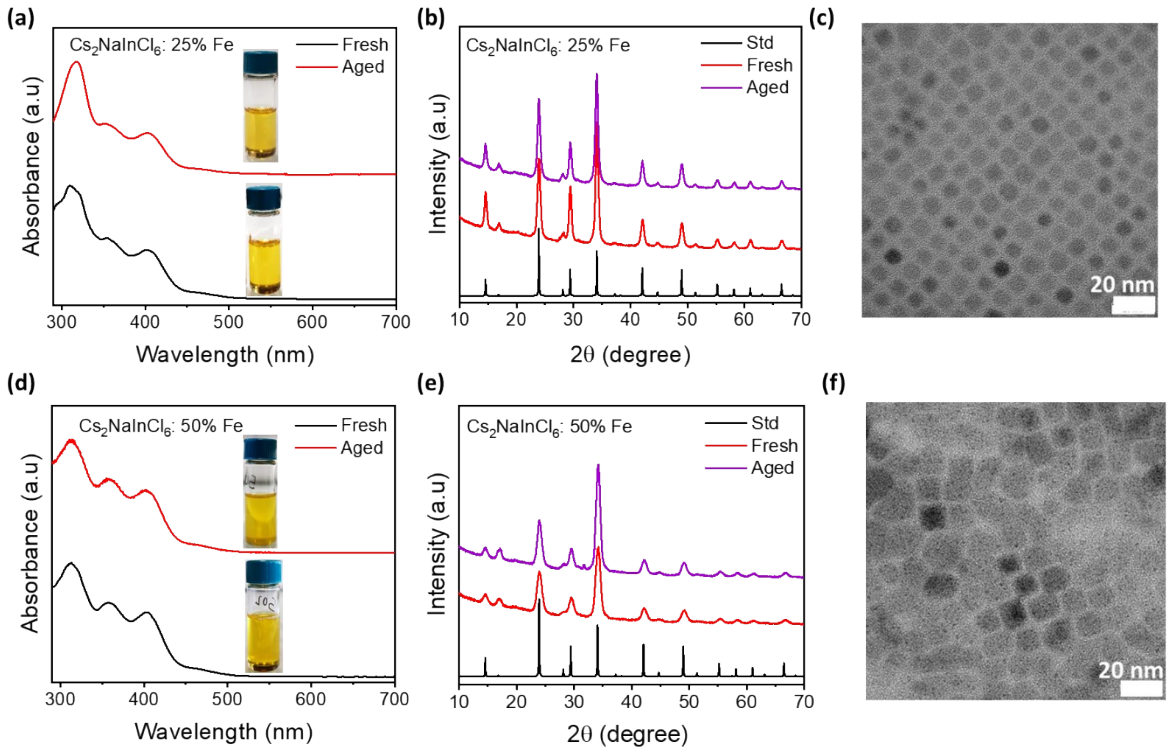

Figure S11. Optical, colloidal, structural, and morphological stabilities of Fe^{3+}-doped $Cs_2NaInCl_6$ NCs which were stored in ambient conditions for 30 days. Absorption spectra of fresh and aged samples (a) with a nominal iron amount of 25%, and (d) with a nominal iron amount of 50%. Inset: Photographs of fresh and aged Fe^{3+}-doped $Cs_2NaInCl_6$ NC solution in toluene with 25% and 50% nominal iron amount presented in the respective figures. (b, e) XRD patterns for fresh and aged samples of Fe^{3+}-doped $Cs_2NaInCl_6$ NC with nominal iron amount of 25% and 50%, respectively, and (c, f) TEM images of aged Fe^{3+}-doped $Cs_2NaInCl_6$ NC with nominal iron amount of 25% and 50%, respectively.

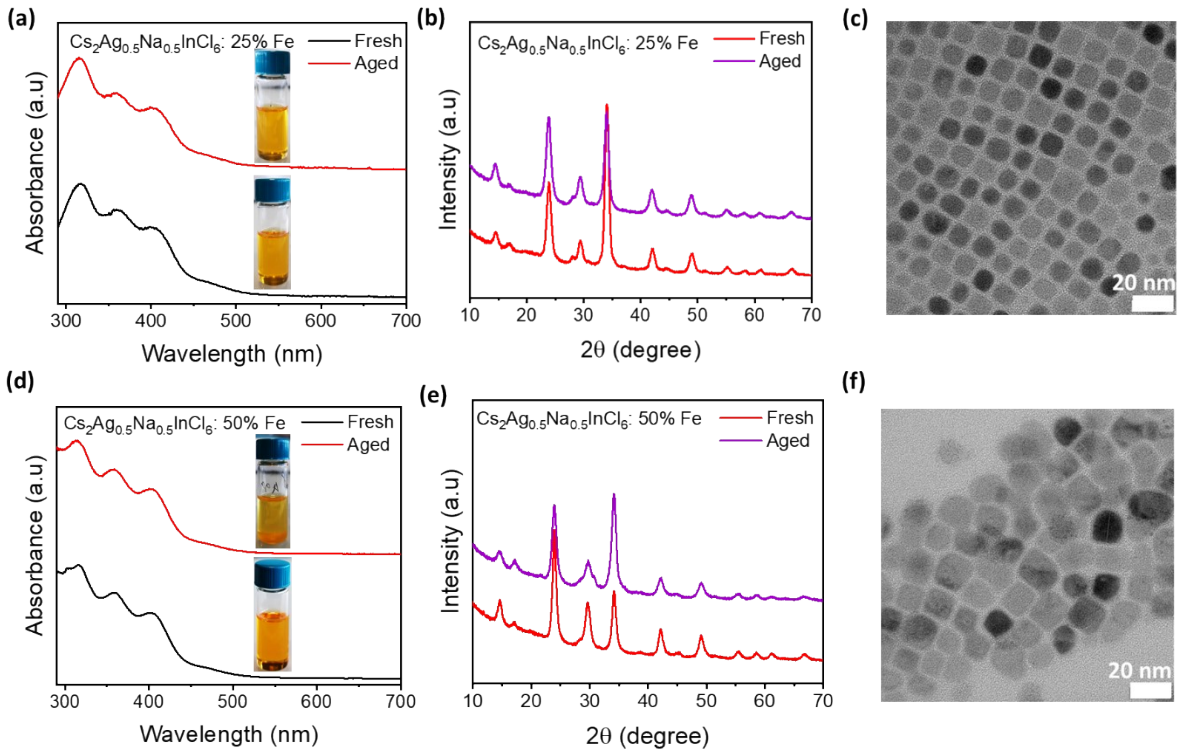

Figure S12. Optical, colloidal, structural, and morphological stabilities of Fe^{3+}-doped $Cs_2Ag_{0.5}Na_{0.5}InCl_6$ NCs which were stored in ambient conditions for 30 days. Absorption spectra of fresh and aged samples (a) with a nominal iron amount of 25%, and (d) with a nominal iron amount of 50%. Inset: Photographs of fresh and aged Fe^{3+}-doped $Cs_2Ag_{0.5}Na_{0.5}InCl_6$ NC solution in toluene with 25% and 50% nominal iron amount presented in the respective figures. (b, e) XRD patterns for fresh and aged samples of Fe^{3+}-doped $Cs_2Ag_{0.5}Na_{0.5}InCl_6$ NC with nominal iron amount of 25% and 50%, respectively, and (c, f) TEM images of aged Fe^{3+}-doped $Cs_2Ag_{0.5}Na_{0.5}InCl_6$ NC with nominal iron amount of 25% and 50%, respectively.

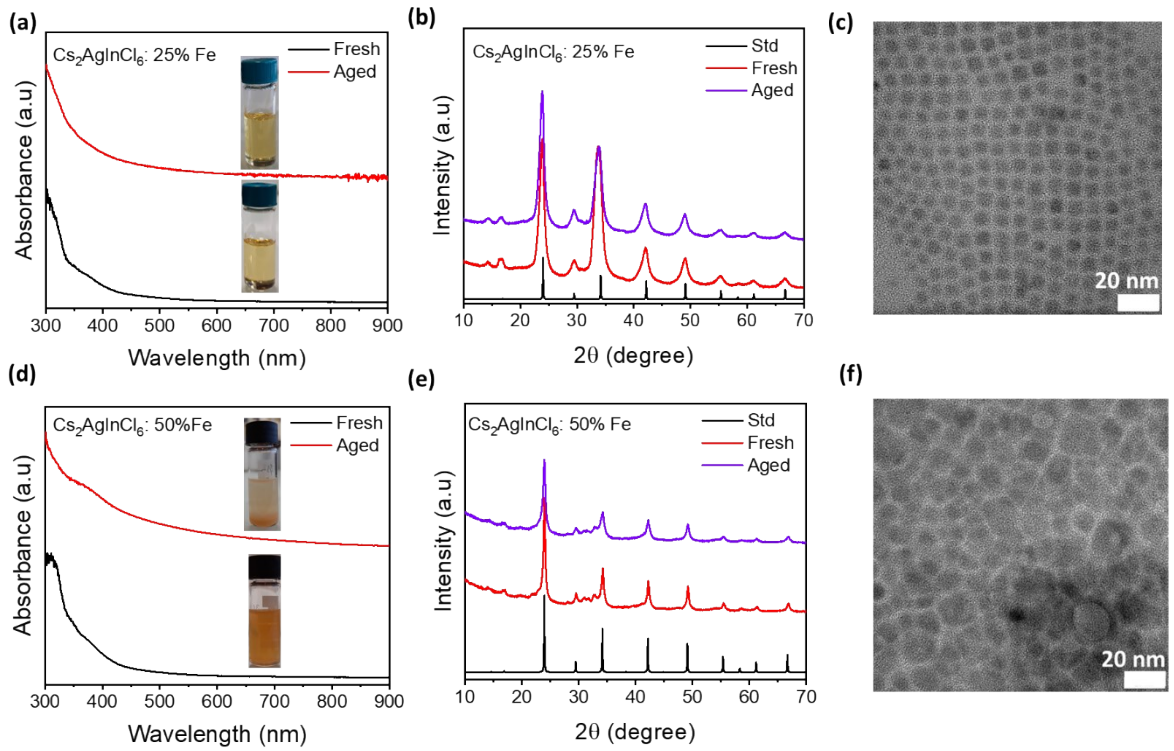

Figure S13. Optical, colloidal, structural, and morphological stabilities of Fe^{3+}-doped $Cs_2AgInCl_6$ NCs which were stored in ambient conditions for 30 days. Absorption spectra of fresh and aged samples (a) with a nominal iron amount of 25%, and (d) with a nominal iron amount of 50%. Inset: Photographs of fresh and aged Fe^{3+}-doped $Cs_2AgInCl_6$ NC solution in toluene with 25% and 50% nominal iron amount presented in the respective figures. (b, e) XRD patterns for fresh and aged samples of Fe^{3+}-doped $Cs_2AgInCl_6$ NC with nominal iron amount of 25% and 50%, respectively, and (c, f) TEM images of aged Fe^{3+}-doped $Cs_2AgInCl_6$ NC with nominal iron amount of 25% and 50%, respectively.

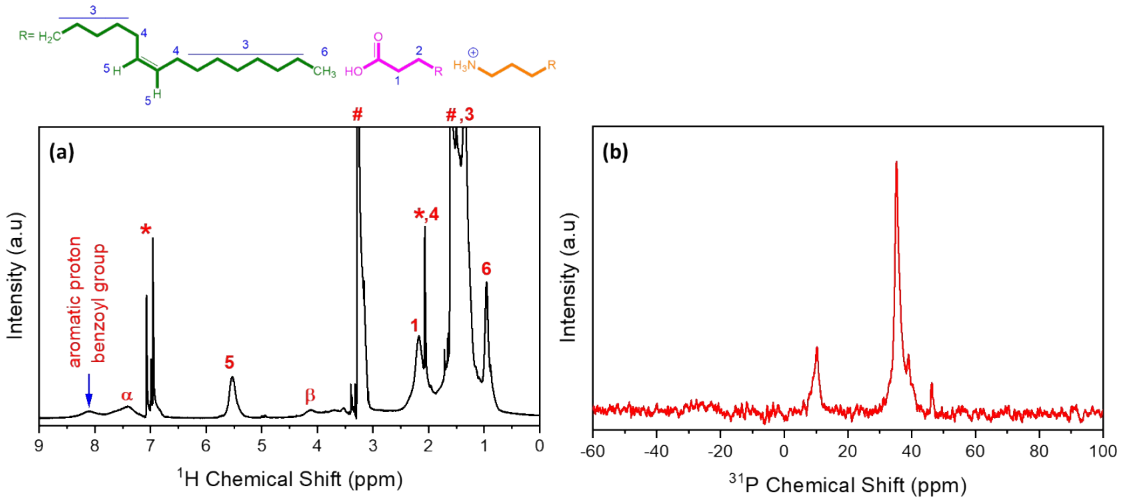

Figure S14. (a) ^1H NMR spectra of extensively washed Fe^{3+}-doped (25% Fe^{3+} nominal loading with respect to In) $Cs_2Ag_{0.5}Na_{0.5}InCl_6$ NCs in toluene-d_8. The characteristic resonance peaks of various protons from OA and OLA are labelled by numbers while peaks for solvent toluene-d_8 (*), methyl acetate (σ) are marked with symbols. The presence broad features from alkene protons at ~5.53 ppm, α protons (at ~7.5 ppm) and β protons (at ~4.1 ppm) of

oleylammonium cations along with peak at 2.2 ppm from proton 1 of OA all verify the binding of OLA and OA to the surface of NCs. (b) ^{31}P NMR spectra of extensively washed Fe^{3+}-doped (25% Fe (III) loading with respect to In) $Cs_2Ag_{0.5}Na_{0.5}InCl_6$ NCs in toluene-d_8.

Table S6. A summary of the photocatalytic CO_2 reduction performances by various Lead-free perovskite photocatalysts

Photocatalyst	Experimental Conditions	Light Source	Products ($\mu mol\ g^{-1}\ h^{-1}$)	References
$Cs_2AgBiBr_6$ NC	Ethyl Acetate	AM 1.5G, 150 mW cm^{-2}	CH_4: 2.3 CO: 1.6	Small, 2018, 14, 1703762
$Cs_2AgBiBr_6$ NPLs	Ethyl Acetate	40 mW 405 nm laser diode	CH_4: 3.8 CO: 6.1	Nano Lett. 2021, 21, 1620−1627
$Cs_2AgBiBr_6$ /g-C_3N_4	Ethyl Acetate + Methanol	150 W Xe lamp	CH_4 + CO 2.0	Appl. Catal. B 2021, 282, 119570.
$Cs_3Sb_2(Br_{0.7}I_{0.3})_9$	CO_2 + H_2O Vapor	300 W Xe lamp, 420 nm	CO: 9.2	Small, 2022, 18, 2106001
$Cs_3Bi_2I_9$	CO_2 + H_2O Vapor	32 W UV Lamp 305 nm	CH_4: 1.5 CO: 7.7	J. Am. Chem. Soc. 2019, 141, 20434
Cs_2SnI_6/SnS_2	CO_2 + H_2O Vapor + Methanol	150 W Xe lamp >400 nm	CH_4: 2.0	J. Am. Chem. Soc. 2019, 141, 13434
$Cs_3Sb_2Br_4Cl_5$	CO_2 + H_2O Vapor	150 mW cm^{-2}	CH_4: 3.0	Adv. Funct. Mater.2023,33, 2303430
$Cs_3Bi_2Br_9/In_4SnS_8$	CO_2 + H_2O Vapor	300 W Xe lamp (λ > 420 nm)	CO: 9.5	*Appl. Catal., B* 2022, *313*, 121426
$Cs_2NaBiCl_6$	CO_2 + H_2O Vapor	300 W Xe lamp	CH_4 + CO 1.1 + 30.2	Adv. Energy Mater. **2022**, 12, 2202074
$Cs_4CuSb_2Cl_{12}$	CO_2 + H_2O Vapor	300 W Xe lamp	CH_4: 0.01 CO: 18.0	Journal of Alloys and Compounds 976 (2024) 173283
$Cs_3Bi_2Br_9$/MOF-525	CO_2 + H_2O Vapor	AM 1.5G, 100 mW cm-2	CH_4: 0.3 CO: 61.3	J. Mater. Chem. A, 2023,11, 4020-4029
$Cs_2AgBiBr_6/Bi_2WO_6$	Ethyl Acetate + Isopropanol	300W Xe Lamp	CH_4: 0.41 CO: 42.1	Journal of Colloid and Interface Science, 2023, 629, 233-242
$Cs_3Bi_2Br_9$@UiO-66	CO_2 + H_2O Vapor	Xe 300W	CH_4: 6.17 CO: 41.7	Small 2024, 2401914
Fe^{3+}-$Cs_2Ag_{0.5}Na_{0.5}InCl_6$ NCs	**Ethyl Acetate + Isopropanol**	**AM 1.5G, 150 mW cm^{-2}, Xe lamp**	**CH_4: 3.0**	**This Work**

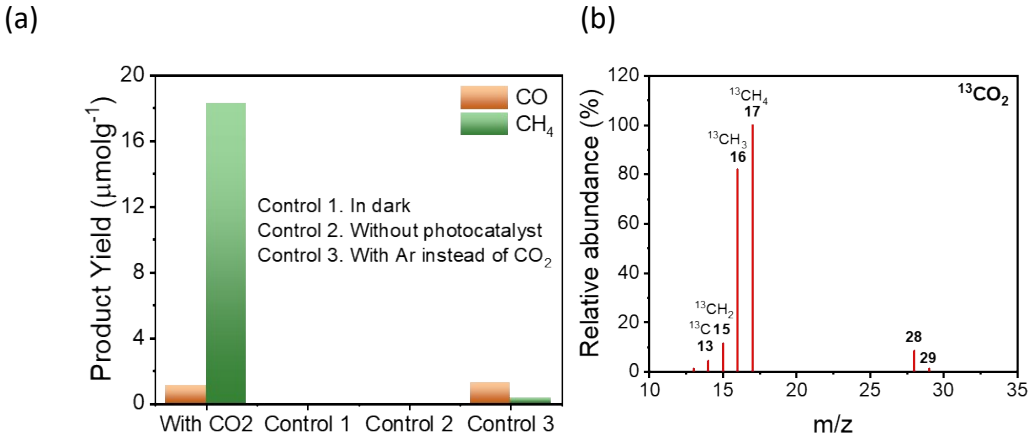

Figure S15. (a) Product yields from the photocatalytic reaction of Fe^{3+}-doped $Cs_2Ag_{0.5}Na_{0.5}InCl_6$ NCs with CO_2 and from control experiments without CO_2 (in Ar atmosphere) after 6h reaction. (b) Mass spectra showing $^{13}CH_4$ (m/z = 17) and ^{13}CO (m/z = 29) generated over Fe^{3+}-doped $Cs_2Ag_{0.5}Na_{0.5}InCl_6$ NCs in $^{13}CO_2$ atmosphere.

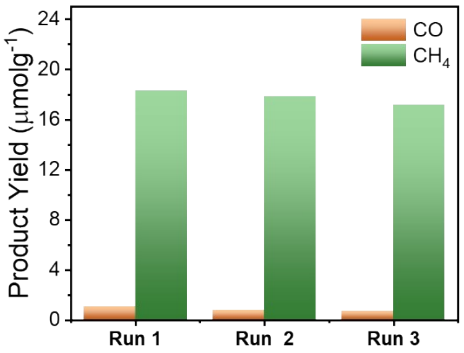

Figure S16. Recycling test of Fe^{3+}-doped $Cs_2Ag_{0.5}Na_{0.5}InCl_6$ NCs for three consecutive runs of 6 h each.

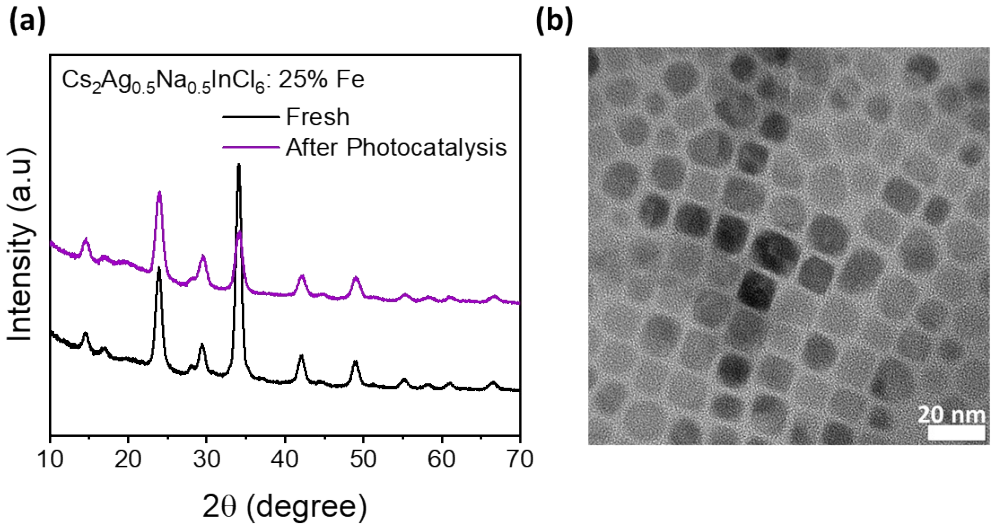

Figure S17. (a) XRD patterns of the Fe^{3+}-doped (25% Fe^{3+} nominal loading with respect to In) $Cs_2Ag_{0.5}Na_{0.5}InCl_6$ NCs before (black) and after (purple) photocatalytic reaction. (b) The TEM image of the NCs after photocatalytic reaction.

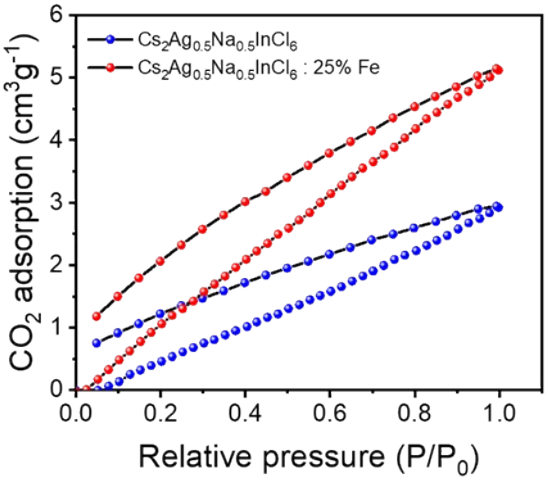

Figure S18. CO_2 adsorption/desorption isotherms of $Cs_2Ag_{0.5}Na_{0.5}InCl_6$ NCs and Fe^{3+}-doped $Cs_2Ag_{0.5}Na_{0.5}InCl_6$ NCs at 298 K

THEORETICAL SECTION

Computational methods. Density functional theory (DFT), implemented in the plane-wave Vienna *ab initio* simulation package (VASP)[1–4], was used to carry out the calculations presented in this paper. The basis set included plane waves with a maximum kinetic energy of 400 eV, and the projected augmented wave (PAW) method[5,6] was used to treat the interactions between ions and electrons, employing GW-optimized PAW potentials. The generalized gradient approximation (GGA) by Perdew-Burke-Ernzerhof (PBE)[7] was used to include the electronic exchange and correlation effects. However, the well-known underestimation of the bandgap values (BG) resulting from the use of the GGA-PBE functional was corrected using the Heyd, Scuseria, and Ernzerhof (HSE03) hybrid functional.[8,9] Calculations for the undoped structure revealed that the use of the HSE06 functional[10] resulted in an overestimation of the BG values (*cf.* Table S7, Figure. S19). Therefore, only the BGs obtained by HSE03 are reported in this work.

The Brillouin zone was typically sampled only at the Γ-point, which is sufficient for calculating the BGs (see Table S7, Figure S19). Decomposed density of states (DOS) were obtained from calculations using at least 3 x 3 x 3 *k*-point mesh or from band structure calculations.

The electronic and magnetic degrees of freedom were relaxed using a preconditioned conjugate gradient algorithm, with an electronic energy convergence threshold set at 10^{-6} eV.

All systems were modelled using a cubic supercell consisting of 8 Cs, 4 Na, 4 In, and 24 Cl (Figure S20). The initial cell dimensions were based on experimental measurements, with a

fixed Cs-Cs distance of 5.26 Å. The supercell allowed for investigation of Ag/Fe doping at 25%, 50%, 75%, and 100%. The effects of geometry relaxation after doping were explored by comparing results obtained in the initial and fully relaxed supercells, where ionic positions and lattice vectors were relaxed simultaneously until the forces acting on each atom were converged to less than 0.025 eV/Å.

The following procedure was used to calculate optical gaps (OG): i/ optimization of the occupied HSE03 orbitals, ii/ optimization of the unoccupied orbitals through direct Hamiltonian optimization, iii/ G_0W_0 calculation[11,12], and iv/ solving the Bethe-Salpeter equation (BSE)[13–15] on top of G_0W_0. Unfortunately, due to limitations in computational resources, the optical gap calculations were carried out at the Γ-point.

The reduction of CO_2 was investigated on a perovskite surface using a slab with the

stoichiometry $Cs_8Na_2Ag_2In_3Fe_1Cl_{24}$, consisting of five layers (similarly to Figure S16 without

the apex Cl atoms) with additional vacuum above the structure. The two bottom layers were

fixed in a bulk-like position, while the remaining layers were allowed to relax. The DFT-D3

method, including van der Waals corrections with a Becke-Johnson damping function[16,17],

was used. In the initial step, the CO_2 molecule was considered at 7 various positions near the

surface Fe atom, and the structure was relaxed at the PBE level until all forces were smaller

than 0.01 eV/Å. The most favourable structure was selected for the subsequent step, in which

Table S7: Calculated electronic bandgap values (in eV) for high-symmetric $Cs_8Na_4In4Cl_{24}$ using various functionals and *k*-point meshes. Bandgap values were determined either by calculating the energy difference between the conduction band edge and valence band edge directly from the difference in eigenvalues (BG_e), or by analyzing the DOS (BG_d) plots, with the latter providing a better representation of bandgaps at non-zero temperatures. BG_e and BG_d are similar but not identical, and for consistency, only BG_e is used in the remainder of the paper as BG.

Functional	*k*-point mesh	BG_e (eV)	BG_d (eV)
PBE	6x6x6	3.31	3.21
HSE06	4x4x4	4.67	4.55
HSE03	1x1x1	4.40	4.19
HSE03	2x2x2	4.40	4.23
HSE03	4x4x4	4.40	4.30
HSE03	6x6x6	4.40	4.35
Exp. value	-	-	4.29

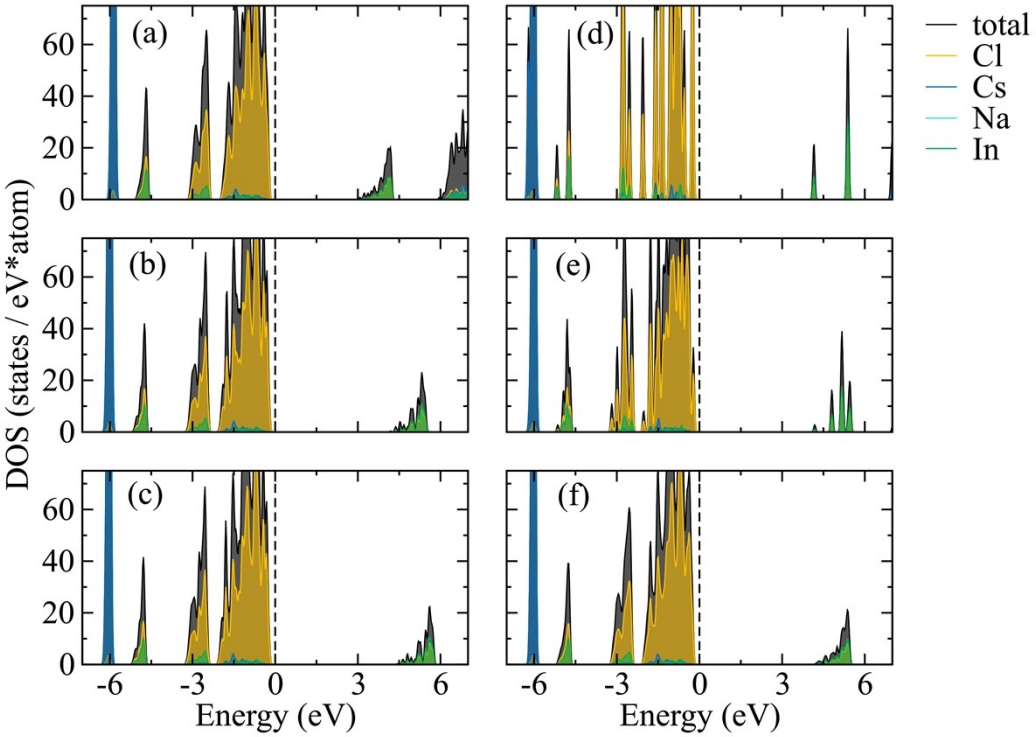

Figure S19: Densities of state (DOS) plots for the initial unrelaxed $Cs_8Na_4In_4Cl_{24}$ supercell, computed using various functionals and k-point meshes: PBE and 6x6x6 (a), HSE03 and 4x4x4 (b), HSE06 and 4x4x4 (c). A convergence test performed for the *k*-point mesh using HSE03: 1x1x1 (d), 2x2x2 (e), 6x6x6 (f). See Table S7 for corresponding electronic band gap values.

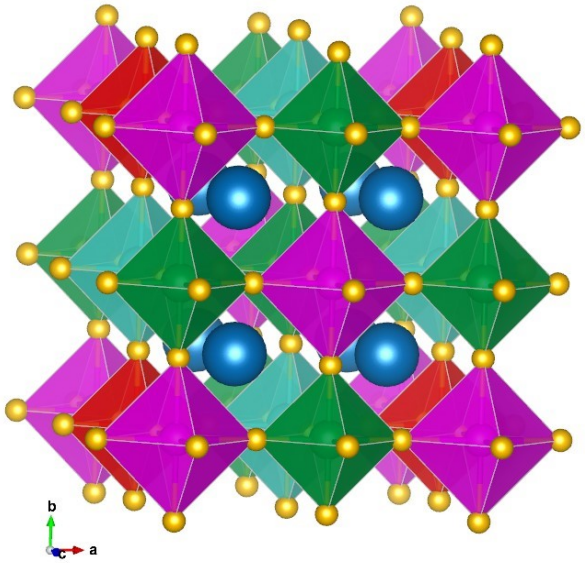

Figure S20: Computational cell of $Cs_8Na_2Ag_2In_3Fe_1Cl_{24}$ with Cs and Cl atoms represented by blue and yellow spheres, respectively. Na, Ag, In, and Fe atoms are in the center of octahedrons of corresponding colors (turquoise, purple, green, and red). Initial supercell is cubic with vertices placed at the centers of the corner purple octahedrons. Relaxations in many systems resulted in tetragonal lattice, but with lattice constants that are very similar.

A hydrogen atom was added to different positions (usually 4-8) around the CO_2 molecule, and the system was relaxed again. Such a loop was repeated until the initial CO_2 molecule fully converted to a CH_4 molecule and two H_2O molecules (the first H_2O molecules was removed after its formation to save computational resources). The energetics of the process were evaluated using the HSE03 functional in subsequent static calculations to correct the well-known drawbacks of GGA-level functionals when adsorbing CO molecules on metals.[18] In our calculations, both PBE and HSE03 predicted similar favourability of the geometry ground state, and the relative energies of various geometries were also similar. Discrepancies between the two functionals occurred only when they converged to different spin isomers, which is beyond the scope of this work to discuss in detail. The effect of solvent was neglected due to the enormous degrees of freedom that would be introduced by an explicit modelling of the ethyl acetate solvent.

Calculations of reference Fe-undoped system were started from the relaxed $Cs_8Na_2Ag_2In_4Fe_0Cl_{24}$ slab with subsequently deposited intermediate products with the same geometry as at the Fe-doped surface; the structures were then relaxed as described above. We expect that the most favourable reaction path is sufficiently covered even by using this resource-conserving approach.

To calculate the Gibbs binding energy, the statistical-thermodynamic procedures described in the book by Christopher J. Crammer[19] was employed. The vibrations of selected parts of the system were limited to C, O, and H atoms.

The internal energy at 0 K (U_0) was obtained from the (hybrid-) DFT total energy (E_{tot}) by adding the zero-point vibrational energy (ZPVE), which is half the sum of the energies of all vibrations (E_i)

$$U_0 = E_{tot} + \frac{1}{2}\sum_{i}^{modes} E_i. \quad (1)$$

The vibrational internal energy (U_{vib}) and the vibrational entropy (S_{vib}) at temperature T can be expressed from the partition function as follows

$$U_{vib} = k_B \sum_{i}^{modes} \frac{E_i}{k_B\left[\exp\left(\frac{E_i}{k_B T}\right) - 1\right]}, \quad (2)$$

where k_B is the Boltzmann constant, and

$$S_{vib} = k_B \sum_{i}^{modes} \left\{ \frac{E_i}{k_B T\left[\exp\left(\frac{E_i}{k_B T}\right) - 1\right]} - \ln\left[1 - \exp\left(-\frac{E_i}{k_B T}\right)\right] \right\}. \quad (3)$$

The internal energy (U) at temperature T is then the sum of U_0 and U_{vib}

$$U = U_0 + U_{vib}. \quad (4)$$

The enthalpy (H) is defined as

$$H = U + pV, \quad (5)$$

where p is pressure and V is volume. Both quantities can be substituted using the equation of state

$$pV = Nk_B T \quad (6)$$

to

$$H = U + k_B T, \quad (7)$$

where N is equal to 1 (since one molecule was investigated at a time), and therefore it is not shown in the final form. Finally, Gibbs energy (G) is calculated from the well-known formula

$$G = H - TS = H - TS_{vib}, \quad (8)$$

since only vibrational entropy has been considered so far.

These equations are satisfactory for supercells that included a surface, which prevents the atoms/molecules from translating and rotating. However, when these degrees of freedom are not restricted, their contributions to the internal energy and entropy must be taken into account. In this case, the equipartition theorem gives

$$U = U_0 + \frac{3}{2}k_B T \quad (9)$$

for a single atom (three translations and zero rotations),

$$U = U_0 + U_{vib} + \frac{5}{2}k_B T \quad (10)$$

for a linear molecule (three translations and two rotations), and

$$U = U_0 + U_{vib} + \frac{6}{2}k_B T \quad (11)$$

for a nonlinear molecule (three translations and three rotations).

The translational entropy (S_{trans}) depends only on the molecular mass (M) and the temperature

$$S_{trans} = k_B\left\{\ln\left[\left(\frac{2\pi M k_B T}{h^2}\right)^{\frac{3}{2}} \cdot \frac{k_B T}{p^0}\right] + \frac{5}{2}\right\} \quad (12)$$

where p^0 is the standard pressure of 101325 Pa. The rotational entropy (S_{rot}) of a linear molecule can be expressed as

$$S_{rot} = k_B\left[\ln\left(\frac{8\pi^2 I k_B T}{\sigma h^2}\right) + 1\right], \quad (13)$$

where σ is a symmetrical factor (1 for asymmetric linear molecules, 2 for symmetric linear molecules), and *I* is the moment of inertia that can be estimated in diatomic molecules as

$$I = \frac{m_1 m_2}{m_1 + m_2} \cdot r^2, \quad (14)$$

where *r* is the distance between the two atoms. The rotational entropy of more complex molecules has been neglected.

Finally, the Gibbs energy (Eq. 8) becomes

$$G = H - TS = H - T\left(S_{vib} + S_{trans} + S_{rot}\right). \quad (15)$$

Structures were visualized using either VESTA[20] or Speck[21]. In Speck, the size of atoms was manually adjusted to distinguish between atoms forming the surface (shown as bigger spheres, visually forming a compact layer) and the C, O, and H atoms (shown in the standard Balls & Stick form). The colour code used in this work was consistent throughout: atoms forming perovskites are described in Figure S20, while C, O, and H atoms are represented by grey, orange, and white spheres, respectively.

Table S8: Calculated electronic band gaps (HSE03) and optical band gaps in eV, at Γ-point of unrelaxed and optimized (Γ-point only, HSE03) high-spin and low-spin Ag- and Fe-doped $Cs_8Na_xAg_{4-x}In_yFe_{4-y}Cl_{24}$. Colours are a guide for the eye. Comparison of experimental and calculated gaps of selected systems. Note that * denotes a manual extension of lattice parameters by 5% in each direction (see the next page).

Electronic band gaps

	Geom. of init. supercell					Relaxed with low-spin Fe					Relaxed with high-spin Fe				
In/Fe ratio \ Na/Ag	4/0	3/1	2/2	1/3	0/4	4/0	3/1	2/2	1/3	0/4	4/0	3/1	2/2	1/3	0/4
4/0	4.40	3.54	2.92	2.66	2.41	4.28		2.87			4.28		2.87		
3/1	2.64	2.40	2.04	2.15	2.33	3.04	2.69	2.51	2.52	2.45	3.05	2.59	2.46	2.43	2.40
2/2	2.51	2.41	2.13	1.95	1.97	2.72	2.36	2.32	2.30	2.16	2.81	2.45	2.28	2.27	2.24
1/3	2.49	2.10	2.13	2.04	2.11			1.64					1.79		
0/4	2.46	2.04	1.98	2.09	2.19			0.76					1.66		

Optical band gaps

	Geom. of init. supercell					Relaxed with low-spin Fe					Relaxed with high-spin Fe				
In/Fe ratio \ Na/Ag	4/0	3/1	2/2	1/3	0/4	4/0	3/1	2/2	1/3	0/4	4/0	3/1	2/2	1/3	0/4
4/0	5.33	4.96	4.66		4.06	5.20		4.52			5.20		4.52		
3/1	3.46		2.77			3.10	3.16	3.23	3.28	3.23	2.92	3.03	3.04	3.16	2.99
2/2	3.36		2.69		2.67	3.12	2.99	3.06	3.12	3.11	2.85	2.94	2.96	3.09	2.93
1/3			2.57					2.49					2.94		
0/4	3.38							2.15					2.86		

Optical properties of selected systems

		Geom. of init. supercell		Relaxed with low-spin Fe		Relaxed with high-spin Fe	
System	Exp. gap	BG	OG	BG	OG	BG	OG
$Cs_8Na_4Ag_0In_4Fe_0Cl_{24}$	4.29	4.40	5.33	4.28	5.20	3.32*	4.43*
$Cs_8Na_4Ag_0In_3Fe_1Cl_{24}$	2.88	2.64	3.46	3.04	3.10	3.05	2.92
$Cs_8Na_4Ag_0In_2Fe_2Cl_{24}$	2.88	2.51	3.36	2.72	3.12	2.81	2.85
$Cs_8Na_4Ag_0In_0Fe_4Cl_{24}$	-	2.46	3.38	-	-	-	-
$Cs_8Na_3Ag_1In_4Fe_0Cl_{24}$	-	3.54	4.96	-	-	-	-
$Cs_8Na_2Ag_2In_4Fe_0Cl_{24}$	4.17	2.92	4.66	2.87	4.52	-	-
$Cs_8Na_2Ag_2In_3Fe_1Cl_{24}$	2.84	2.04	2.77	2.51	3.23	2.46	3.04
$Cs_8Na_2Ag_2In_2Fe_2Cl_{24}$	2.84	2.13	2.69	2.32	3.06	2.28	2.96
$Cs_8Na_2Ag_2In_1Fe_3Cl_{24}$	-	2.13	2.57	-	-	-	-
$Cs_8Na_0Ag_4In_4Fe_0Cl_{24}$	4.13	2.41	4.06	-	-	-	-
$Cs_8Na_0Ag_4In_2Fe_2Cl_{24}$	2.7	1.97	2.67	-	-	-	-

Electronic and optical band gaps

Structural-optical properties

Table S8 shows that the theoretical optical gaps in several systems may typically overestimate the experimental ones by 10-20%. However, our tests (Figure S21) indicated that manually increasing the pre-optimized lattice parameter by up to 5% can correct the optical band gap and bring it into at-least semi-qualitative agreement with experimental values, as demonstrated for the pristine $Cs_8Na_4In_4Cl_{24}$. These findings highlight the pivotal role of accurate geometries in optoelectronic properties calculations. It should be noted that the current study did not involve detailed investigations of structural-optical properties, which would be necessary to accurately determine optical band gaps that match experimental gaps. Such analyses require significant computational resources and were not feasible within the scope of this work.

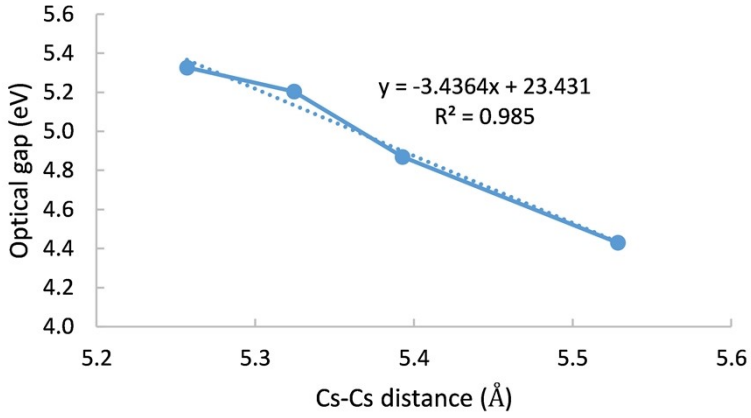

Figure S21: Negative correlation between the optical band gap and lattice constant (measured as the Cs-Cs distance) in pristine $Cs_8Na_4In_4Cl_{24}$. The optical calculations were conducted in systems with the lattice extended by hand from the initial geometry (only atomic positions were relaxed within the initial lattice) optimized at the HSE03 level (Cs-Cs: 5.257 Å), up to an extension of ~2.5 % (Cs-Cs: 5.393 Å) and ~5 % (Cs-Cs: 5.529 Å). Optical band gap lying above the trend connection corresponds to the fully optimized geometry (lattice and atomic positions) at the HSE03 level (Cs-Cs: 5.325 Å).

Effect of geometry optimization on the electronic structure of Fe- and Ag- doped DPs

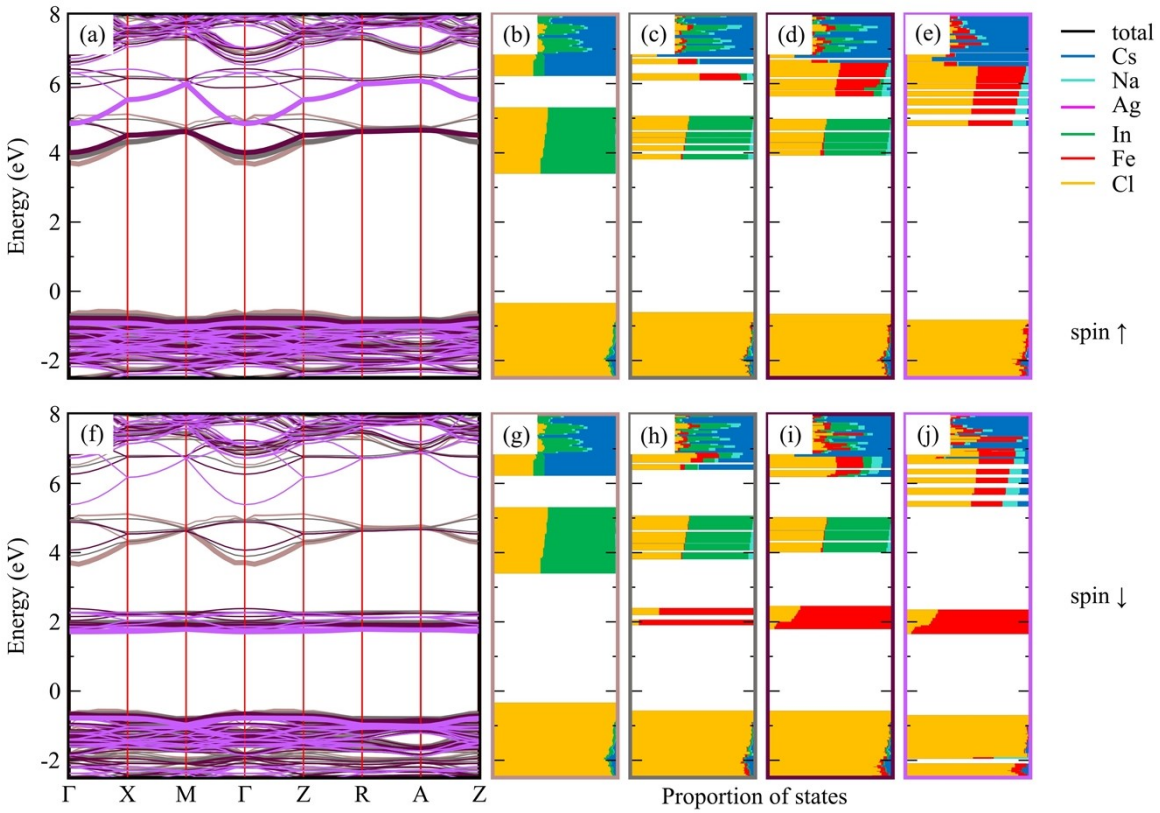

Figure S23: Spin-resolved electronic band structure of the initial unrelaxed supercell of high-spin Fe-doped $Cs_8Na_4In_yFe_{4-y}Cl_{24}$ with the valence and conductive band edges marked with bold lines (a, f). The colors in the band structure plot match the colors in the corresponding DOS plots shown in (b-e) and (g-j). DOS plots of $Cs_8Na_4In_4Fe_0Cl_{24}$ (b, g), $Cs_8Na_4In_3Fe_1Cl_{24}$ (c, h), $Cs_8Na_4In_2Fe_2Cl_{24}$ (d, i), and $Cs_8Na_4In_0Fe_4Cl_{24}$ (e, j).

The level of Fe^{3+} doping has only a negligible effect on BGs in both spin configurations.

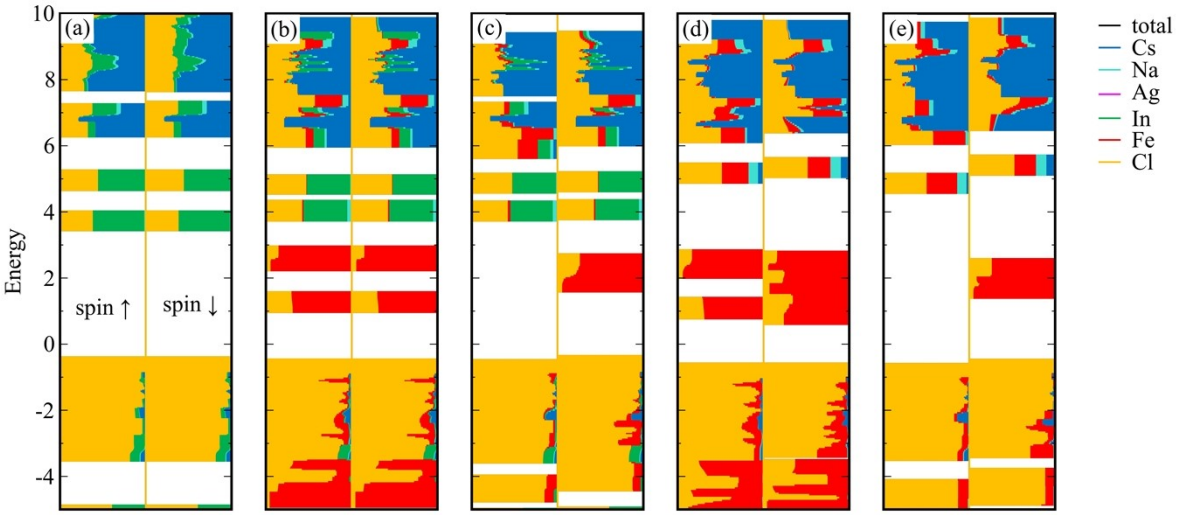

Figure S22: Spin-resolved DOS plots calculated at the Γ-point for unrelaxed Fe-doped $Cs_8Na_4In_xFe_{4-x}Cl_{24}$, including $Cs_8Na_4In_4Fe_0Cl_{24}$ (a), low- (b) and high-spin (c) isomers of $Cs_8Na_4In_2Fe_2Cl_{24}$ and low- and high-spin isomers of $Cs_8Na_4In_0Fe_4Cl_{24}$ (d, e). The colors in the plot correspond to the elements shown in the legend.

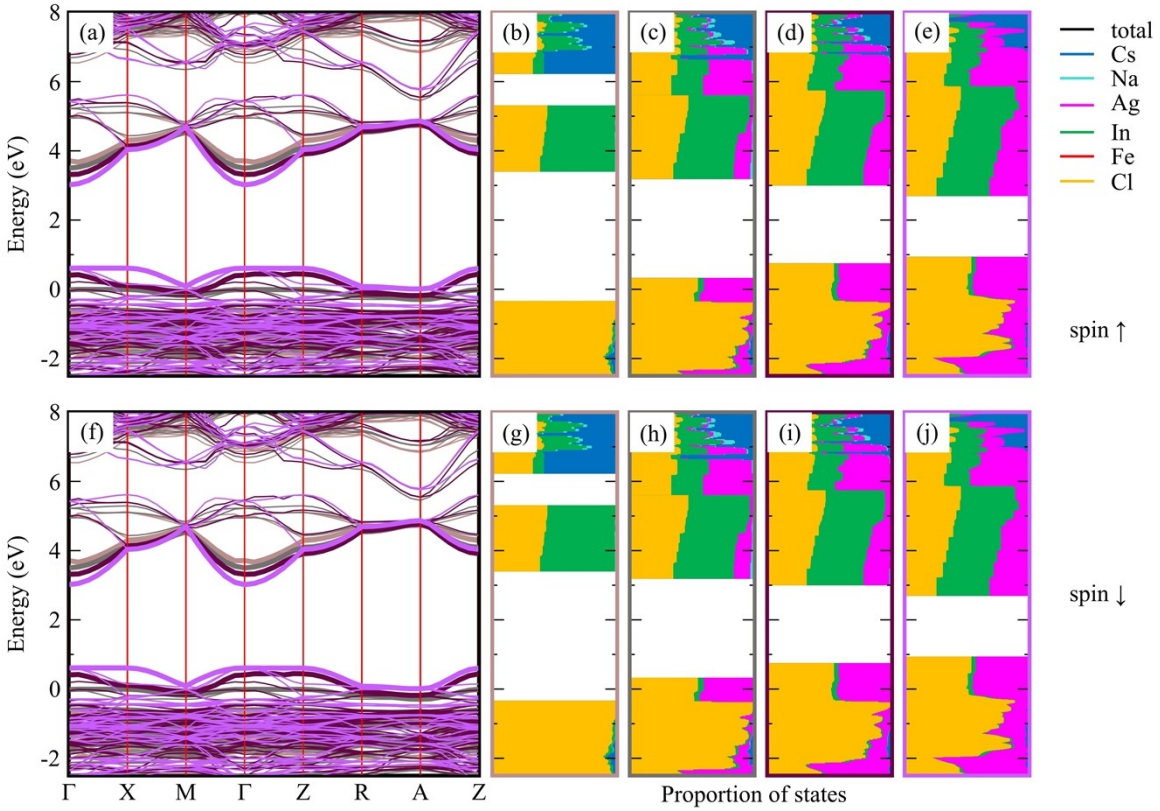

Figure S24: Spin-resolved electronic band structure of the initial unrelaxed Ag-doped $Cs_8Na_xAg_{4-y}In_4Cl_{24}$ supercell, with the valence and conductive band edges marked with bold lines (a, f). The colors in the band structure plot match the colors in the corresponding DOS plots shown in (b-e) and (g-j). DOS plots of $Cs_8Na_4Ag_0In_4Cl_{24}$ (b, g), $Cs_8Na_3Ag_1In_4Cl_{24}$ (c, h), $Cs_8Na_2Ag_2In_4Cl_{24}$ (d, i), and $Cs_8Na_0Ag_4In_4Cl_{24}$ (e, j). To sample the reciprocal space, a regular 3 x 3 x 3 *k*-point mesh was employed, which was also used for the DOS plots. To sample paths in the band structures, additional zero-weighted *k*-points were added.

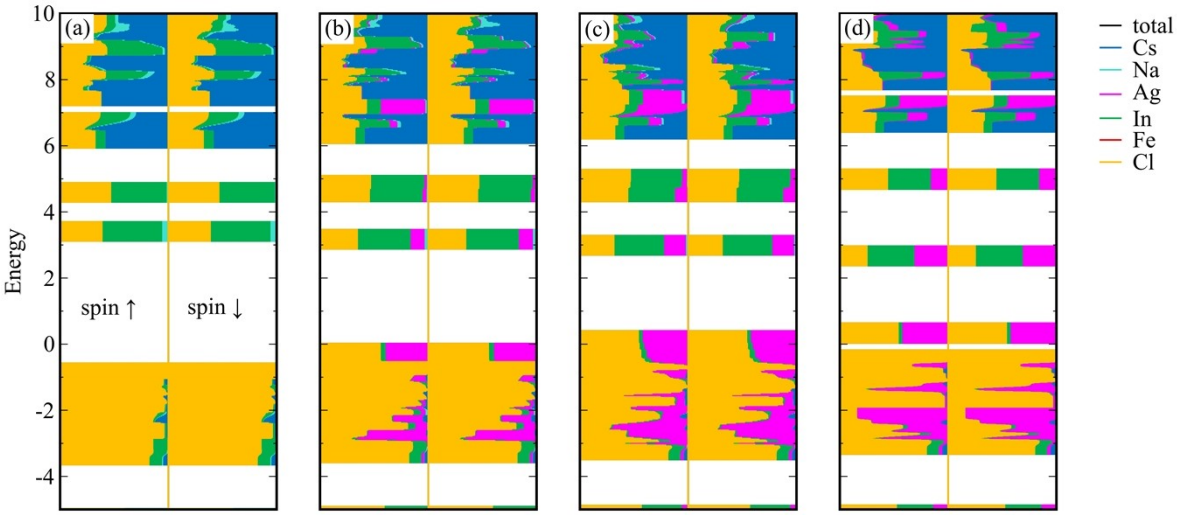

Figure S25: Spin-resolved DOS plots calculated at the Γ-point for relaxed Ag-doped $Cs_8Na_xAg_{4-x}In_4Cl_{24}$. $Cs_8Na_4Ag_0In_4Cl_{24}$ (a), $Cs_8Na_3Ag_1In_4Cl_{24}$ (b), $Cs_8Na_2Ag_2In_4Cl_{24}$ (c), $Cs_8Na_0Ag_4In_4Cl_{24}$ (d). The colors in the plot correspond to the elements shown in the legend.

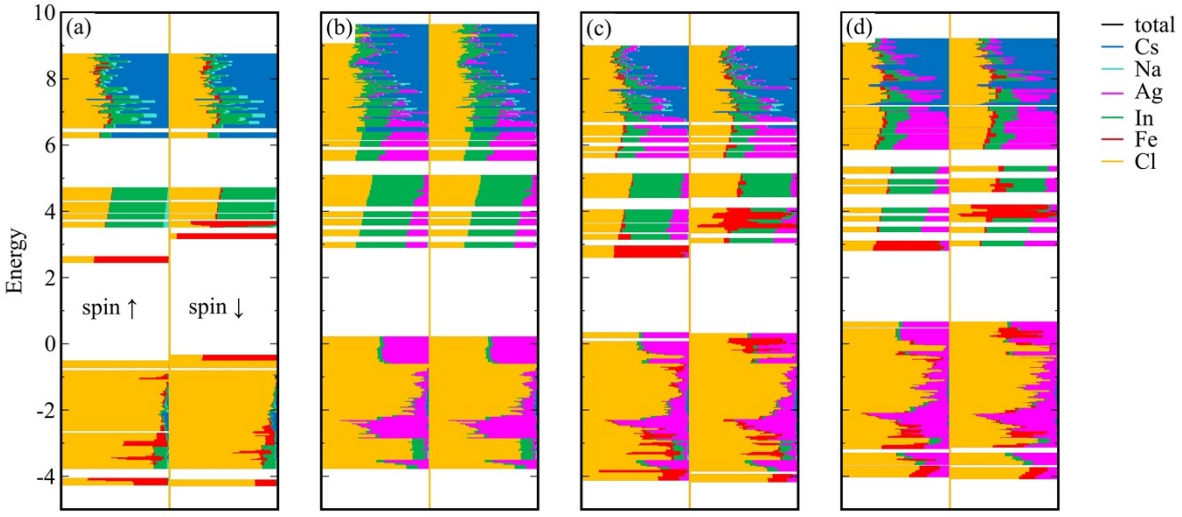

Figure S26: Spin-resolved DOS plots for the HSE03-optimized $Cs_8Na_2Ag_2In_4Fe_0Cl_{24}$ supercell, and the low-spin $Cs_8Na_4In_3Fe_1Cl_{24}$ doped with Ag with a constant In/Fe ratio: $Cs_8Na_4Ag_0In_3Fe_1Cl_{24}$ (a), $Cs_8Na_2Ag_2In_4Fe_0Cl_{24}$ (b), $Cs_8Na_2Ag_2In_3Fe_1Cl_{24}$ (c), and $Cs_8Na_0Ag_4In_3Fe_1Cl_{24}$ (d). Compare with Figure 3 in the main text.

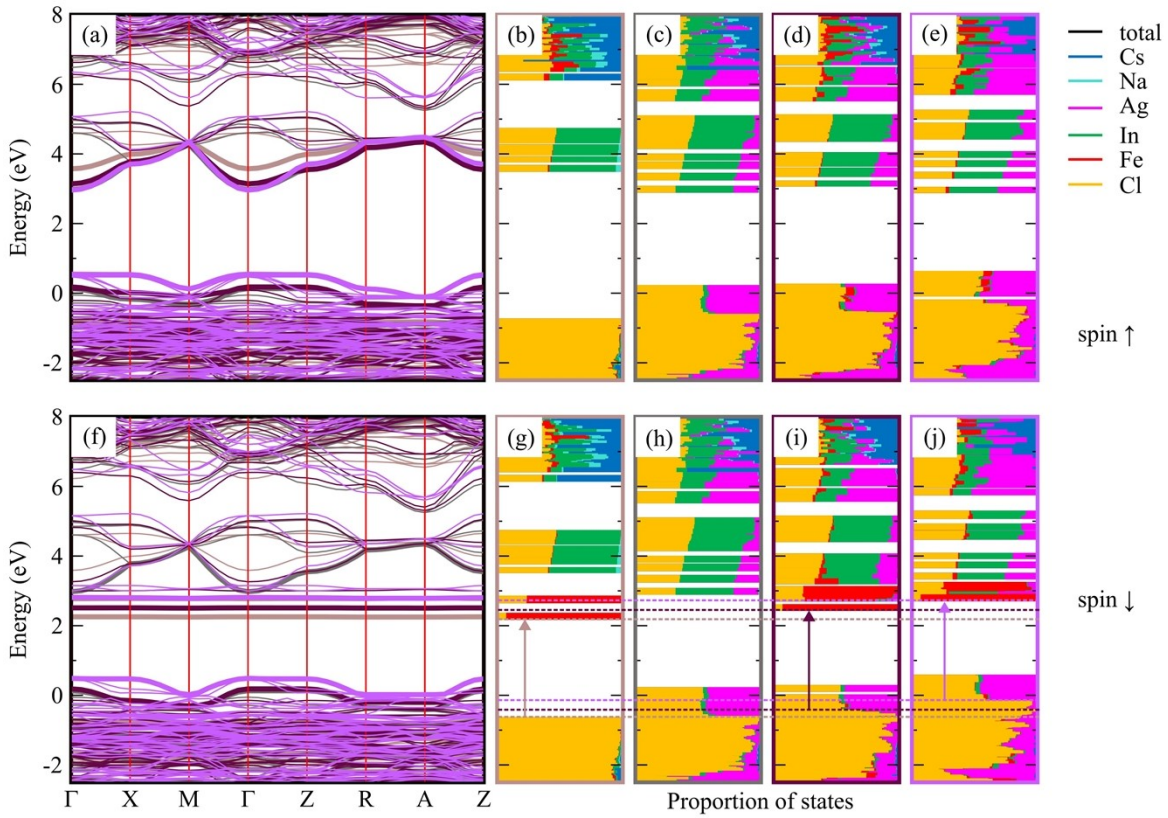

Figure S27: Electronic structure of Fe-doped $Cs_8Na_4In_3Fe_1Cl_{24}$ and the effect of Ag-doping with a constant In/Fe ratio. (a, f) Spin-resolved electronic band structure with colors corresponding to the bounding boxes of the DOS plots shown in (b-e) and (g-j). Valence and conductive band edges are marked with bold lines. DOS plots (see also Figure S26) of $Cs_8Na_4Ag_0In_3Fe_1Cl_{24}$ (b, g), $Cs_8Na_2Ag_2In_4Fe_0Cl_{24}$ (c, h), $Cs_8Na_2Ag_2In_3Fe_1Cl_{24}$ (d, i), and $Cs_8Na_0Ag_4In_3Fe_1Cl_{24}$ (e, j). Arrows indicate the most probable transitions corresponding to the optical gap, and the edges of these transitions are marked by dashed horizontal lines. Compare with Figure. 3 in the main text, which shows the low-spin configuration. The relaxed reference system without Fe is $Cs_8Na_2Ag_2In_4Fe_0Cl_{24}$.

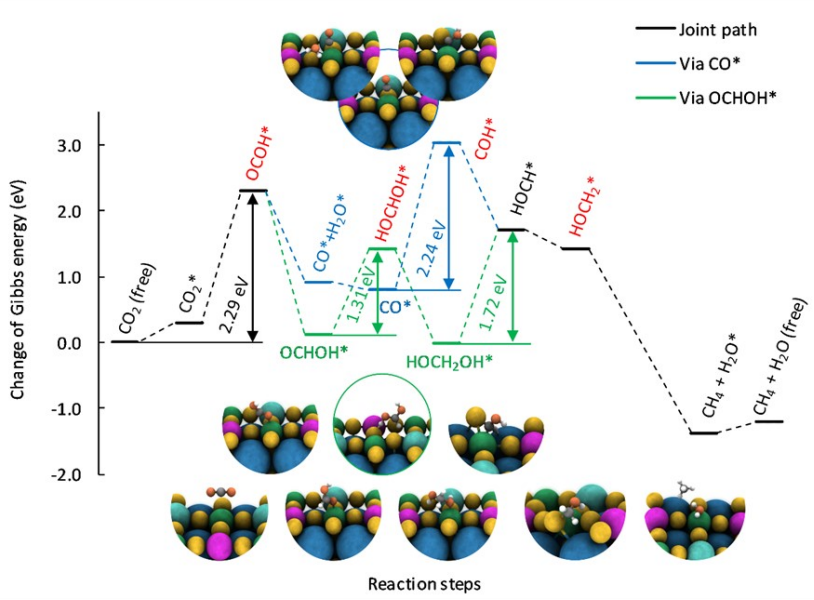

Figure S28: Energy profile for the reduction of CO_2 on the $Cs_8Na_2Ag_2In_4Fe_0Cl_{24}$ surface together with corresponding geometries. The Gibbs energies are relative to the Gibbs energy of a free CO_2 molecule and free surface.

References

(1) Kresse, G.; Hafner, J. Ab Initio Molecular Dynamics for Liquid Metals. *Physical Review B* **1993**, *47* (1), 558–561.

(2) Kresse, G.; Hafner, J. Ab Initio Molecular-Dynamics Simulation of the Liquid-Metal–Amorphous-Semiconductor Transition in Germanium. *Physical Review B* **1994**, *49* (20), 14251–14269.

(3) Kresse, G.; Furthmüller, J. Efficiency of Ab-Initio Total Energy Calculations for Metals and Semiconductors Using a Plane-Wave Basis Set. *Computational Materials Science* **1996**, *6* (1), 15–50.

(4) Kresse, G.; Furthmüller, J. Efficient Iterative Schemes for Ab Initio Total-Energy Calculations Using a Plane-Wave Basis Set. *Physical Review B* **1996**, *54* (16), 11169–11186.

(5) Blöchl, P. E. Projector Augmented-Wave Method. *Physical Review B* **1994**, *50* (24), 17953–17979.

(6) Kresse, G.; Joubert, D. From Ultrasoft Pseudopotentials to the Projector Augmented-Wave Method. *Physical Review B* **1999**, *59* (3), 1758–1775.

(7) Perdew, J. P.; Burke, K.; Ernzerhof, M. Generalized Gradient Approximation Made Simple. *Physical Review Letters* **1996**, *77* (18), 3865–3868.

(8) Heyd, J.; Scuseria, G. E.; Ernzerhof, M. Hybrid Functionals Based on a Screened Coulomb Potential. *The Journal of Chemical Physics* **2003**, *118* (18), 8207–8215.

(9) Heyd, J.; Scuseria, G. E. Efficient Hybrid Density Functional Calculations in Solids: Assessment of the Heyd–Scuseria–Ernzerhof Screened Coulomb Hybrid Functional. *The Journal of Chemical Physics* **2004**, *121* (3), 1187–1192.

(10) Krukau, A. V.; Vydrov, O. A.; Izmaylov, A. F.; Scuseria, G. E. Influence of the Exchange Screening Parameter on the Performance of Screened Hybrid Functionals. *The Journal of Chemical Physics* **2006**, *125* (22), 224106.

(11) Shishkin, M.; Kresse, G. Implementation and Performance of the Frequency-Dependent G W Method within the PAW Framework. *Phys. Rev. B* **2006**, *74* (3), 035101.
(12) Fuchs, F.; Furthmüller, J.; Bechstedt, F.; Shishkin, M.; Kresse, G. Quasiparticle Band Structure Based on a Generalized Kohn-Sham Scheme. *Phys. Rev. B* **2007**, *76* (11), 115109.
(13) Salpeter, E. E.; Bethe, H. A. A Relativistic Equation for Bound-State Problems. *Phys. Rev.* **1951**, *84* (6), 1232–1242.
(14) Albrecht, S.; Reining, L.; Del Sole, R.; Onida, G. *Ab Initio* Calculation of Excitonic Effects in the Optical Spectra of Semiconductors. *Phys. Rev. Lett.* **1998**, *80* (20), 4510–4513.
(15) Rohlfing, M.; Louie, S. G. Electron-Hole Excitations in Semiconductors and Insulators. *Phys. Rev. Lett.* **1998**, *81* (11), 2312–2315.
(16) Grimme, S.; Antony, J.; Ehrlich, S.; Krieg, H. A Consistent and Accurate *Ab Initio* Parametrization of Density Functional Dispersion Correction (DFT-D) for the 94 Elements H-Pu. *The Journal of Chemical Physics* **2010**, *132* (15), 154104.
(17) Grimme, S.; Ehrlich, S.; Goerigk, L. Effect of the Damping Function in Dispersion Corrected Density Functional Theory. *J. Comput. Chem.* **2011**, *32* (7), 1456–1465.
(18) Stroppa, A.; Termentzidis, K.; Paier, J.; Kresse, G.; Hafner, J. CO Adsorption on Metal Surfaces: A Hybrid Functional Study with Plane-Wave Basis Set. *Phys. Rev. B* **2007**, *76* (19), 195440.
(19) Cramer, C. J. *Essentials of Computational Chemistry: Theories and Models*, 2nd ed.; Wiley: Chichester, West Sussex, England ; Hoboken, NJ, 2004.
(20) Momma, K.; Izumi, F. VESTA 3 for Three-Dimensional Visualization of Crystal, Volumetric and Morphology Data. *Journal of Applied Crystallography* **2011**, *44* (6), 1272–1276.
(21) Terrell, R. Speck. https://github.com/wwwtyro/speck.